Supporting Information

Unlocking Nanotubular Bismuth Oxyiodide toward Carbon-Neutral Electrosynthesis

Peng-Fei Sui[a], Min-Rui Gao[a], Meng-Nan Zhu[a], Chenyu Xu[a], Yi-Cheng Wang[a], Subiao Liu[b], Jing-Li Luo[a,c]*

[a] Department of Chemical and Materials Engineering, University of Alberta, Edmonton, Alberta T6G 1H9, Canada

[b] School of Minerals Processing and Bioengineering, Central South University, Changsha, Hunan, 410083, P.R. China

[c] Shenzhen Key Laboratory of Polymer Science and Technology, College of Materials Science and Engineering, Shenzhen University, Shenzhen 518060, Guangdong, China

*Corresponding author: Jing-Li Luo

Telephone: +1 780 492 2232

Email: jingli.luo@ualberta.ca

S1. Specifications of Chemicals and Gases

Bismuth nitrate pentahydrate ($Bi(NO_3)_3 \cdot 5H_2O$), potassium iodide (KI), sodium hydroxide (NaOH), polyvinylpyrrolidone (PVP10, Mw. 10000), hydrazine monohydrate (N_2H_4 64-65%), ammonia solution (32%), potassium hydroxide (KOH), sodium chloride (NaCl), potassium bicarbonate ($KHCO_3$) and Nafion perfluorinated ion-exchange resin solution (5 wt% in mixture of lower aliphatic alcohol and H_2O) were purchased from Sigma-Aldrich. Phenolphthalein and ethanol were purchased from Fisher Scientific. Toray carbon paper (Toray TGP-H-060) and Nafion® N-117 membrane (0.18 mm thick) were purchased from Fuel Cell Store. Deionized water was produced and taken from a Millipore Autopure system. All chemicals were used without further purification. Hydrogen (H_2, 99.99%), argon (Ar, 99.999%), compressed air (extra dry) and carbon dioxide (CO_2, 99.999%) were purchased from Praxair.

S2. Experimental section

S2.1 Catalyst fabrication

Synthesis of Bi_5O_7I nanotubes and nanobelts

Bi_5O_7I nanotubes were prepared via the hydrothermal method. First, 2 mmol $Bi(NO_3)_3 \cdot 5H_2O$ and 3.2 g PVP were added into 40 mL deionized water under stirring condition to form a uniform solution. Then, 20 mL KI-saturated solution was added dropwise into the precursor solution with continuous stirring and red solution was formed. After stirring for 10 minutes, the NaOH solution (3 M) was added into the mixture to adjust the pH to 10.5. Subsequently, the resulting solution mixture was transferred into a 100 mL Teflon-line stainless steel autoclave and heated at 160 ℃ for 3 hours. After cooling down to room temperature, the products were collected by centrifugation and washed with DI water and ethanol four times respectively to remove the residuals. The obtained product was dried at 60 °C overnight before further usage. Bi_5O_7I nanobelts were prepared with the same procedure except adjusting the pH to 12.5.

Synthesis of Bi nanotubes

Bismuth nanotubes were prepared via the hydrothermal method. First, 2.5 mmol $Bi(NO_3)_3 \cdot 5H_2O$ and 5 mmol hydrazine monohydrate were added into deionized water under stirring to form the precipitate. Then, the pH value was adjusted to 12.5 using ammonia solution. After stirring for 30 min, the mixture was transferred to a 100 mL Teflon-line stainless steel autoclave and heated at 120 °C for 12 h. After cooling down to room temperature, the products were collected by centrifugation and washed with diluted hydrochloric acid and DI water and four times respectively. The obtained product was dried at 60 °C in vacuum oven overnight before further usage.

S2.2 Material Characterizations

The X-ray diffraction measurements were performed on Rigaku Ultima IV with a Cu Kα source at 40 kV and 44 mA with a scan speed 2° min^{-1}. The morphology of materials was obtained by using a field-emission scanning electron microscope (Zeiss Sigma FESEM). Transmission electron microscopy (TEM), high-angle annular darkfield scanning transmission electron microscopy (HAADF-STEM) and energy-dispersive X-ray spectroscopy (EDS) analyses were conducted on a JEOL JEM-ARM200cF S/TEM with a cold field-mission gun and a probe spherical aberration corrector at an accelerating voltage of 200 kV. The contact angle measurement was conducted using Contact Angle (FTA-200). The electron paramagnetic resonance (EPR) was acquired using Bruker A300 EPR Spectrometer. The work function was measured by the ultraviolet photoelectron spectroscopy (UPS). with a Kratos AXIS Ultra photoelectron spectrometer using He I (21.2 eV) ultraviolet radiation and pass energy of 10 eV. Each sample has a distinct Fermi edge for various V_{bias} values, and by extrapolating the cut-off energies to $V_{bias}= 0$, we then determined the work function values.

S2.3 Electrochemical measurements

Electrochemical measurements in H-type cell

The electrochemical measurements were performed with an electrochemical interface (Solartron 1287) and an impedance/gain-phase analyzer (Solartron 1255). For each kind of catalyst, three-electrode cell was used for measurements for the performance and product analyses to ensure the repeatability. The error ranges are derived by calculating the deviations from the average Faradaic efficiencies, the mean values for all the measurements at each applied potential. The electrochemical measurement was carried out with a typical three-electrode H-type cell, where the saturated calomel electrode (SCE) and graphite rod served as reference electrode and counter electrode, respectively. Before measurement, each compartment of cell was filled with 40 ml electrolyte. CO_2 was bubbled into the 0.5M $KHCO_3$ solution at a flow rate of 20 ml min^{-1} for at least 30 minutes before each experiment to remove all the oxygen and achieve a saturated CO_2 condition. All the potentials versus SCE were recorded and converted the reversible hydrogen electrode (RHE) reference scale by the equation:

$$E(\text{V vs. RHE}) = E(\text{V vs. SCE}) + 0.241 + 0.0592\text{pH}$$

Liner sweep voltammetry (LSV) curves were recorded at a scan rate of 20 mV s^{-1}. Electrochemical impedance spectroscopy (EIS) measurements were carried out at -1.0 V vs. RHE in CO_2-saturated 0.5 M $KHCO_3$ aqueous solution with a three-electrode configuration with the AC voltage signal of a 10 mV amplitude over the frequency range 0.1-10^5 Hz.

The electrochemically active surface area (ECSA) of a material with similar composition is proportional to its electrochemical double-layer capacitance (C_{dl}), which was measured by CV in a non-Faradaic region at the different scan rates (V_s) of 40, 60, 80, 100, 120 mV s^{-1}. Then, the C_{dl} was determined by plotting the $\Delta j=(j_a-j_c)/2$ at -0.25 V vs. SCE as a function of the scan rate.

The ECSA can be calculated from the C_{dl} according to:

$$ECSA = \frac{C_{dl}}{C_s}$$

where C_s is the specific capacitance of a flat surface with 1 cm^2 of real surface area. Here, the average double-layer capacitance of a smooth metal surface is assumed to be 20 μF cm^{-2}. The calculated value of ECSA for Bi_5O_7I NTs was about 340.5 cm^2, while the value for Bi_5O_7I NBs was 163 cm^2.

Electrochemical measurements in flow cell and MEA system

The flow cell was constructed with gas diffusion electrode (GDE) and a Pt foil as the cathode and the anode, respectively, separated by the anion exchange membrane. The Hg/HgO (1.0 M KOH) electrode was used as the reference electrode. To prepare the GDE, 10 mg of electrocatalyst and 10 mg of carbon black (Vulcan XC 72R) were mixed and the solvent containing 800 μl ethanol and 200 μl Nafion solution was added. After sonication for 3 h, the prepared ink was drop-cast onto carbon paper with a loading mass of 0.5 mg cm^{-2} and stored to dry in air for 24 h before measurement. All the potentials versus Hg/HgO electrode were recorded and converted the RHE reference scale by the equation:

$$E \text{ (V vs. RHE)} = E \text{ (V vs. Hg/HgO, 1.0 M KOH)} + 0.098 \text{ V} + 0.0592 \text{ pH}$$

The flow rate of CO_2 gas was 20 mL min^{-1}. The electrolyte of 1.0 M KOH was circulated in both cathode and anode with a flow rate of 10 mL min^{-1} pumped by Precision Peristaltic Pump (BINACA PUMPS).

The custom-built two-electrode MEA system consisting of titanium plates with serpentine flow channels was used to evaluate the CO_2RR performance. The cathode and anode were separated by an anion exchange membrane (Sustainion X37-50 Grade RT. Dioxide Materials). The humidified CO_2 was fed into the cathode at 50 mL min^{-1} controlled by the mass flow controller, while the anode was circulated with 0.1 M $KHCO_3$ electrolyte at a rate of 5 mL min^{-1}. The cathode was prepared using the same method as flow cell preparation. The anode was prepared by depositing IrO_2 on a titanium mesh support by a dip coating followed by calcination. Liquid product FE was calculated by considering the total amount of the products collected from anode and cathode sides in the same period.

S2.4 Products analysis

Gas products analysis

The gas products from cathode were identified by an online Hewlett-Packard model Agilent 6890N gas chromatograph (GC) equipped with a packed bed column (HaySep D) operated at 100 °C with a thermal conductivity detector and a flame ionization detector. Argon was used as the carrier gas with a flow rate of 30 ml min^{-1}. At each applied potential, the cathodic gas was injected into GC three times with an interval of 6 min to get the average value of the products. Faradaic efficiency of gas products can be calculated as follows:

$$\mathrm{FE}_{Product} = \frac{F n_{product} v_{product} f_v p_0}{R T_0 I_{total}} \times 100\%$$

where F is the Faradaic constant; $n_{product}$ is the number of mole of electrons participating in the reaction to form certain product; $v_{product}$ is the volume concentration of certain product in the exhaust gas from the cell; f_v is the flow rate of the exhaust gas measured at the exit of the cell at room temperature (T_0) and ambient pressure (p_0); I_{total} is the total current of the steady cell.

Liquid products analysis

The liquid product of formic acid was measured three times at each applied potential by using 850 Professional IC-AnCat-MCS with Metrosep Organic Acids-250/7.8 column. The eluent was 0.5 mmol L^{-1} sulfuric acid mixed with 10% acetone with the standard flow rate of 0.5 mL min^{-1}. The Faradaic efficiency of formic acid can be calculated by using the following equation:

$$\mathrm{FE}_{formate} = \frac{2c_{(formate)}VF}{Q_{total}} \times 100\%$$

where $c_{(formate)}$ is the concentration of formic acid determined by IC; V is the total volume of electrolyte in cathode chamber; F is the Faradaic constant; Q_{total} is the total amount of charge passing through the system.

The formate formation rate is calculated using the equation below:

$$Formation\ Rate = \frac{Q_{total} \times FE_{formate}}{F \times N_{formate} \times t \times S}$$

where $N_{formate}$ is the number of moles of the produced formate in a period of time t; S is the surface area of the electrode with the catalyst.

S2.5 *In situ* electrochemical Raman spectroscopy measurement

The in situ electrochemical Raman spectroscopy was conducted using a Renishaw inVia Qontor Confocal Rman Microscope. As the excitation source, a laser of 532 nm (50 mW) was used. The monochromator was calibrated before each set of measurements using the zero-order peak and the Si lattice peak at 520.5 cm^{-1} of a Si wafer reference sample. The measurement was conducted in a three-electrode electrochemical cell made by polytetrafluoroethylene (PTFE) with a quartz window. The spectra were measured from the open circuit potential (OCP) to cathodic potentials (V vs. RHE). The cathodic limit is defined by the interference of HER because the formation of bubbles on the electrode leads to the signal loss. Before measurement, the CO_2 gas was bubbled through the electrolyte for 30 minutes to ensure that the solution reached saturation. Each spectrum was accumulated for 1 min after the 10 min electrolysis, allowing the system to achieve a steady-state condition after each change of potential.

S3. Density functional theory (DFT) calculation

Density functional theory (DFT) calculations were performed by Vienna Ab initio Simulation Package (VASP) [1-3]. In order to treat the electron-ion interaction and exchange-interaction, projector-augmented plane-wave (PAW) [3, 4] method and Perdew-Burke-Ernzerhof (PBE) [5] function were utilized, respectively. The cut-off energy has been set at 520eV and the spin polarization were switched on for all the elements. A (3×3) surface model with six atomic layers were built based an optimized unit cell of Bi. To avoid the interaction between neighbouring slabs, a vacuum layer with at least 15 Å were added. Monkhorst-Pack (4×4×1) were set for k points sampling of Brillouim zone. A Gaussian smearing of 0.2 eV was employed for optimization of surface geometries while it was set at 0.01 eV for gas-phase species. The degree of ions relaxation was not terminated until a maximum force component of 0.05eV/Å was achieved. Different geometries of surface with and without the adsorption of intermediates were considered and the one with the lowest electronic energy was chosen. During the surface optimization, the first three atomic layers were fully relaxed while the other layers were fully fixed. The k points sampling of Brillouin zone was increased to Monkhorst-Pack (12×12×1) for determination of partial density of states. The software packages named "p4vasp" and "VESTA" were employed for output data processing to get the partial density of states and charge transfer between *OCHO intermediate and Bi surface. The Bi surface model with one Bi vacancy is denoted as "Mono-Bi (Bi-V_1)" and the Bi surface model with two Bi vacancies is Monkhorst-Pack denoted as "Dino-Bi (Bi-V_2)". Based on equation 1 shown below, a gibbs free energy diagram for CO_2RR was built.

$$G=E_{DFT}+ZPE+\int C_p dT-TS \qquad \text{(Eq.1)}$$

Here, the DFT calculated electronic energy, zero-point energy, enthalpy correction and entropy correction are represented by E_{DFT}, ZPE, $\int C_p dT$ and -TS individually. Contributions from PV was neglected. 3N freedom degrees were treated as frustrated harmonic vibrations to calculate ZPE and enthalpy correction while a proposed standard method was used to calculate entropy contribution and transfer it to thermodynamic data at room temperature [6, 7]. The computational hydrogen electrode (CHE) model [8] describing each electrochemical reaction step as a simultaneous transfer of proton and electron was employed. CO_2RR is divided into three steps as shown in equations (2) to (4) where * represents corresponding surface where intermediates were adsorbed.

$$*+CO_2+2(H^++e^-) = *OCHO+(H^++e^-) \qquad \text{(Eq.2)}$$

$$*OCHO+(H^++e^-) = *HCOOH \qquad \text{(Eq.3)}$$

$$*HCOOH = *+ HCOOH \qquad \text{(Eq.4)}$$

The initial state in which H_2O molecular is freely above clean surface is taken as the reference. Therefore, the Gibbs free energy change of each step is expressed in Eq. (5-7).

$$\Delta G[*OCHO]=G[*OCHO]-G[H^++e^-]-G[*]-G[CO_2] \qquad \text{(Eq.5)}$$

$$\Delta G[*HCOOH]=G[*HCOOH]-2G[H^++e^-]-G[*]-G[CO_2] \qquad \text{(Eq.6)}$$

$$\Delta G[HCOOH]=G[HCOOH]-2G[H^++e^-]-G[*]-G[CO_2] \qquad \text{(Eq.7)}$$

The hydrogen evolution reaction (HER) is written as $H^++e^-=0.5H_2$. Based on CHE model, the Gibbs free energy of (H^++e^-) is expressed in Eq. 8.

$$G[H^++e^-] = 0.5G[H_2]-G[*] \qquad \text{(Eq.8)}$$

The CO_2RR for CO route can be divided into three steps as shown in Eq. (9-11),

$$CO_2 + * + 2(H^+ + e^-) \leftrightarrow *COOH + H^+ + e^- \quad \text{(Eq.9)}$$

$$*COOH + H^+ + e^- \leftrightarrow *CO + H_2O \quad \text{(Eq.10)}$$

$$*CO + H_2O \leftrightarrow * + CO + H_2O \quad \text{(Eq.11)}$$

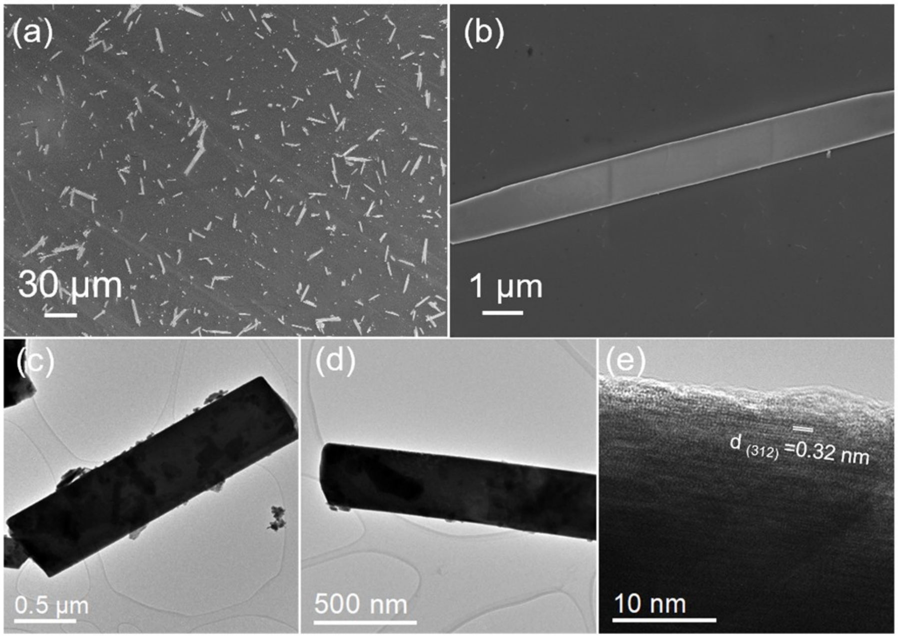

Figure S1. (a) and (b) SEM images, (c) and (d) TEM images and (e) HRTEM image of Bi_5O_7I NBs.

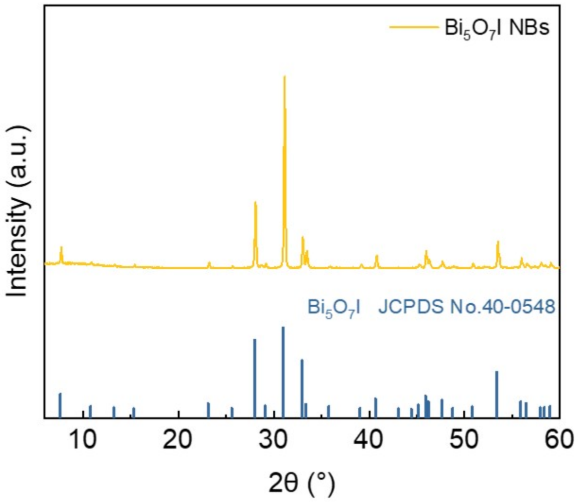

Figure S2. XRD pattern of Bi_5O_7I NBs.

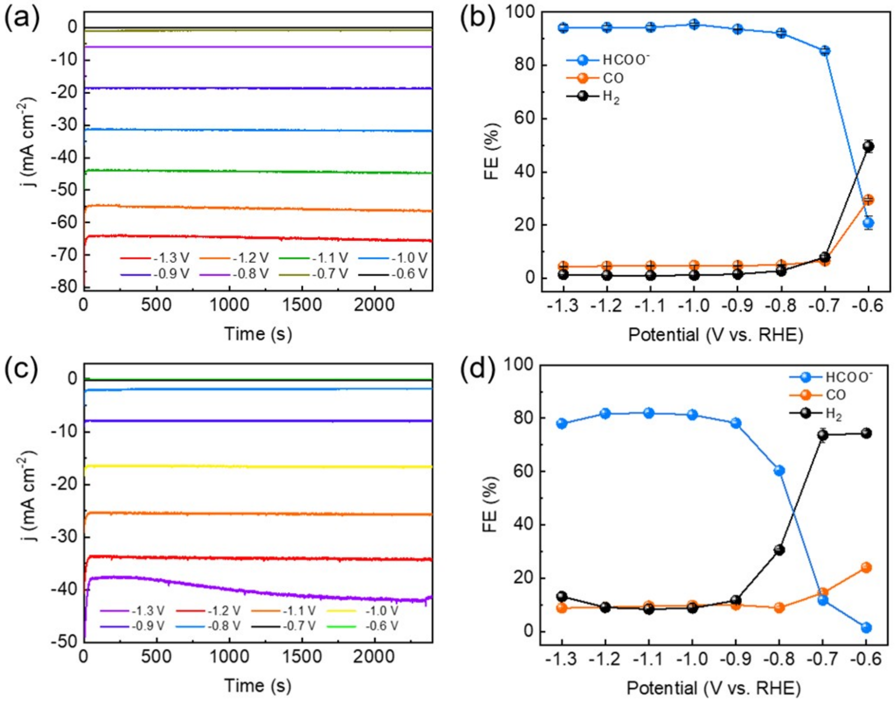

Figure S3. Plots of current densities as a function of time and Faradaic efficiencies at different potentials for (a) and (b) Bi_5O_7I NTs; (c) and (d) Bi_5O_7I NBs.

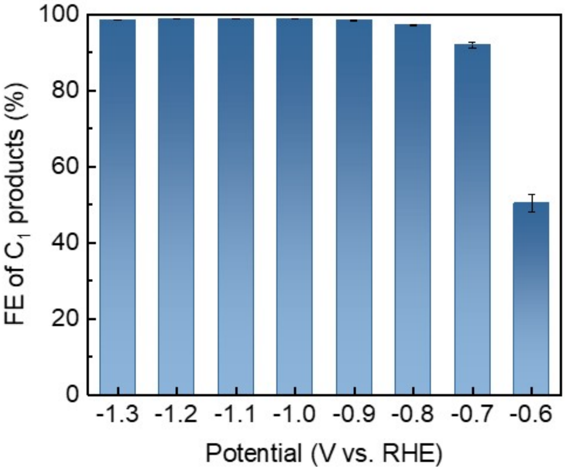

Figure S4. FEs of C_1 products on Bi_5O_7I NTs at different applied potentials.

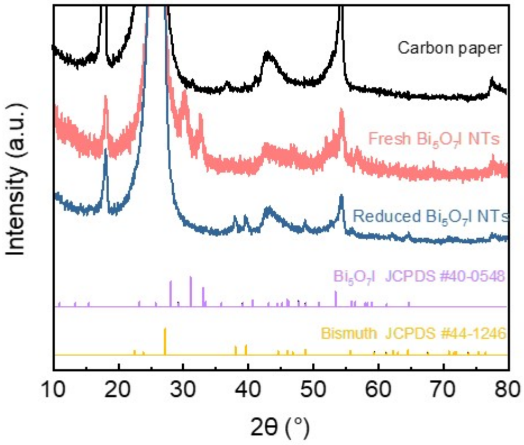

Figure S5. XRD result of Bi_5O_7I NTs after CO_2RR measurements.

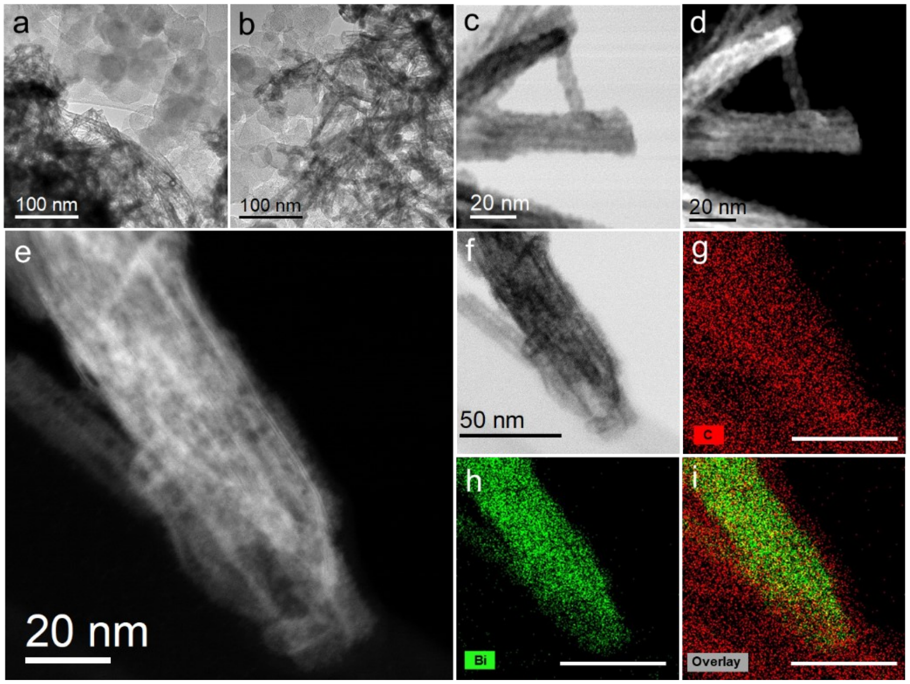

Figure S6. (a) and (b) TEM images; (c) to (f) HAADF-STEM and BF-STEM images; (g) to (i) the corresponding EDS elemental mappings of Bi_5O_7I NTs after CO_2RR stability measurements.

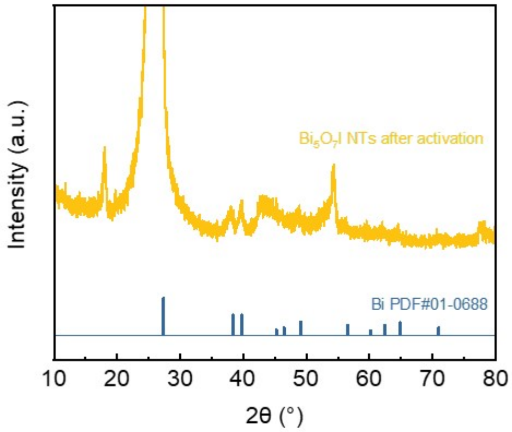

Figure S7. XRD result of Bi_5O_7I NTs after activation at −1.0 V in 0.5 M CO_2-saturated $KHCO_3$ electrolyte.

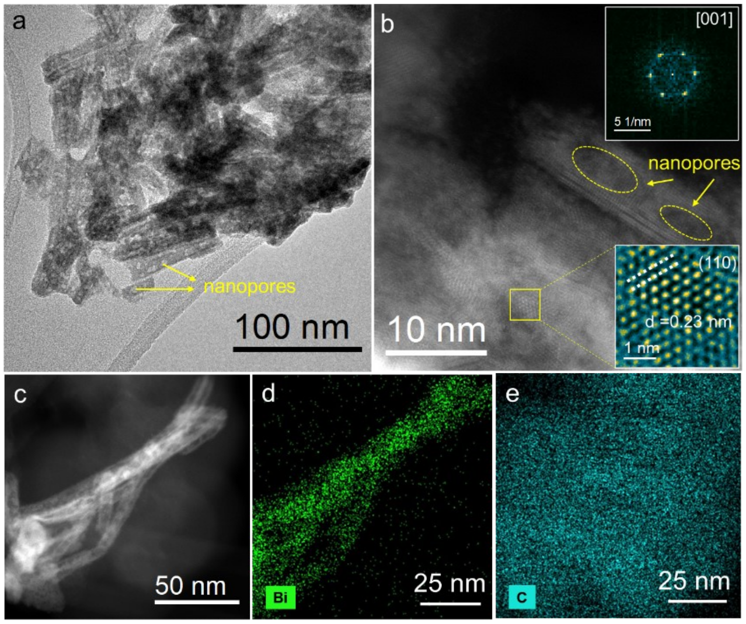

Figure S8. (a) HRTEM image; (b) and (c) HAADF-STEM images (insert: Fourier transform pattern and enlarged lattice image of selected area); (d) and (e) the corresponding elemental mappings of Bi_5O_7I NTs after activation at −1.0 V in 0.5 M CO_2-saturated $KHCO_3$ electrolyte.

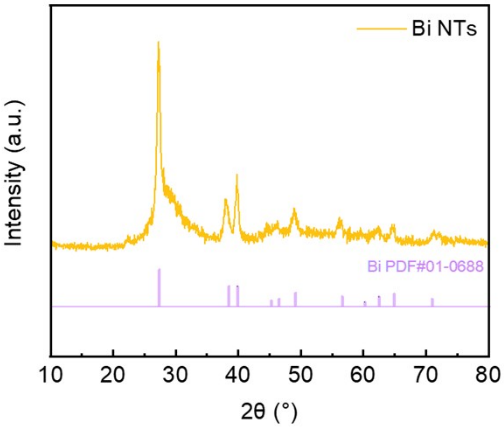

Figure S9. XRD pattern of the synthesized Bi NTs.

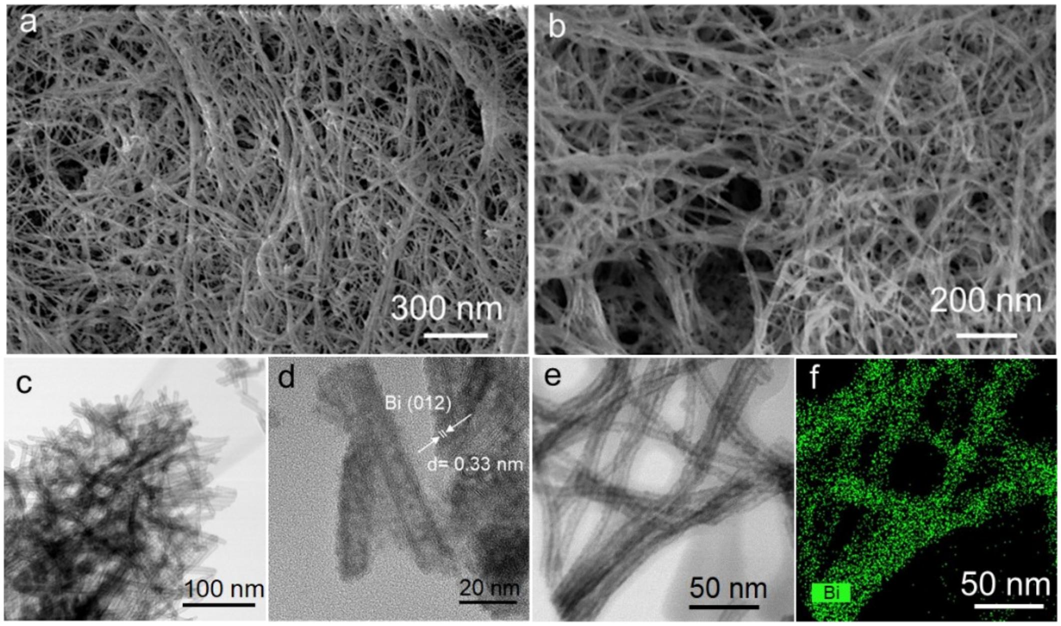

Figure S10. (a) and (b) SEM images; (c) TEM image; (d) HRTEM image; (e) BF-STEM images and (f) EDS elemental mapping of the prepared Bi NTs.

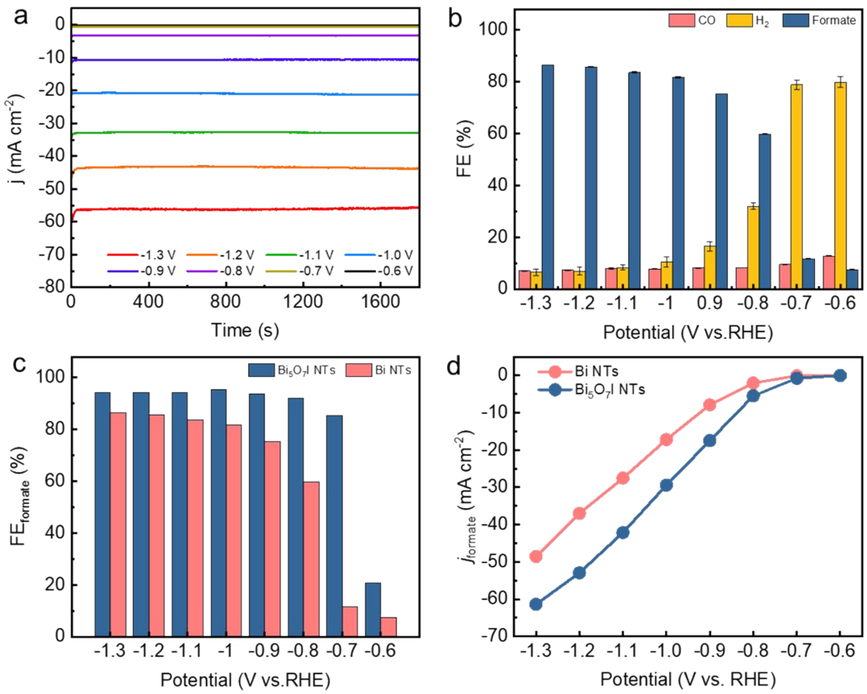

Figure S11. (a) Plots of current densities as a function of time; (b) Faradaic efficiencies at different potentials; (c) $FE_{formate}$ and (d) $j_{formate}$ comparison with Bi_5O_7I NTs.

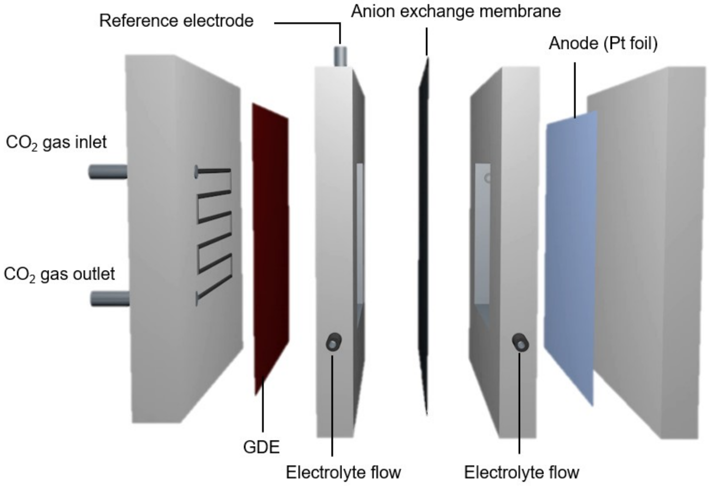

Figure S12. Schematic illustration of the flow cell configuration.

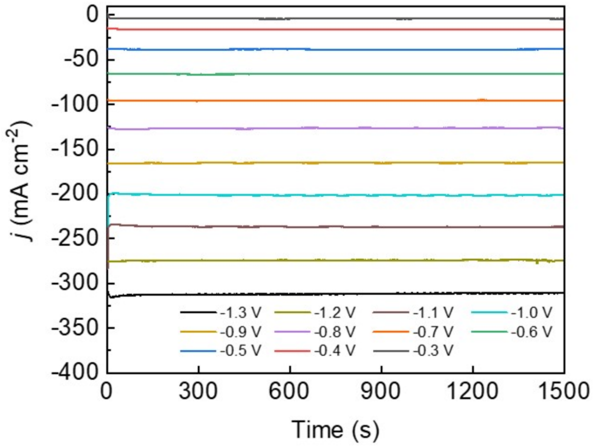

Figure S13. Plots of current densities as a function of time at different potentials in the flow cell.

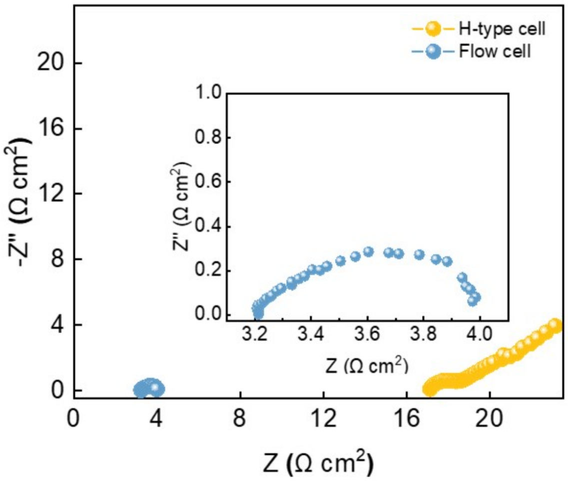

Figure S14. Nyquist plots of Bi_5O_7I NTs (inset: the enlarge result in flow cell) in the H-type cell and flow cell.

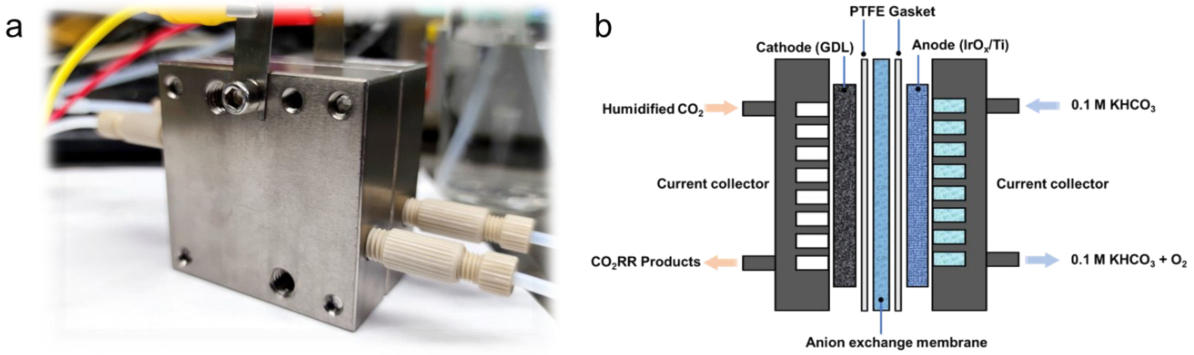

Figure S15. (a) Photo of custom-built membrane electrode assembly system; (b) The schematic diagram of MEA.

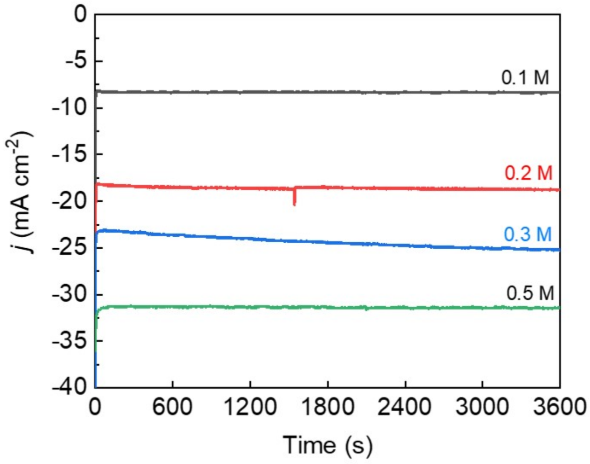

Figure S16. Plot of current densities as a function of time in different concentrations of CO_2-saturated $KHCO_3$ at -1.0 V vs. RHE.

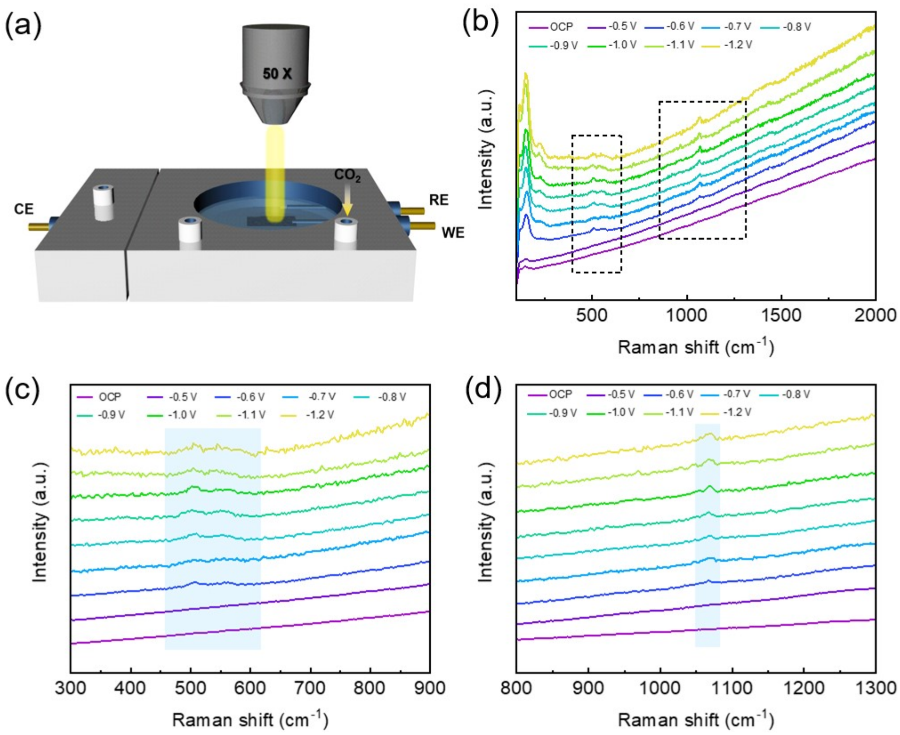

Figure S17. (a) Schematic illustration of the *in situ* Raman measurement device for CO_2RR, (b), (c) and (d) Potential-dependent Raman spectra on Bi_5O_7I NTs in 0.5 M CO_2-saturated $KHCO_3$.

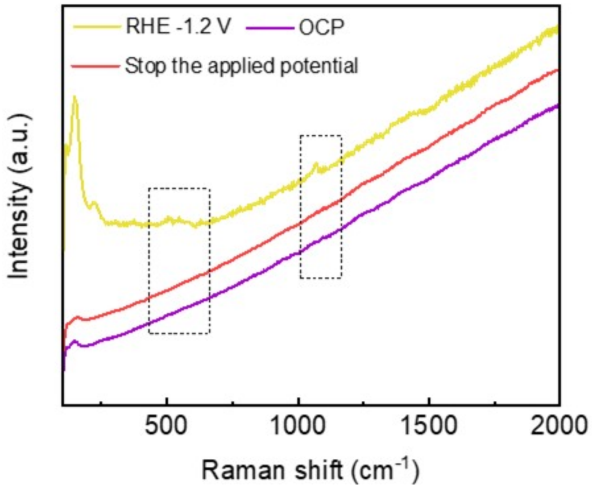

Figure S18. The measured Raman spectra (red) of Bi_5O_7I NTs after stopping the applied potential for 5 minutes.

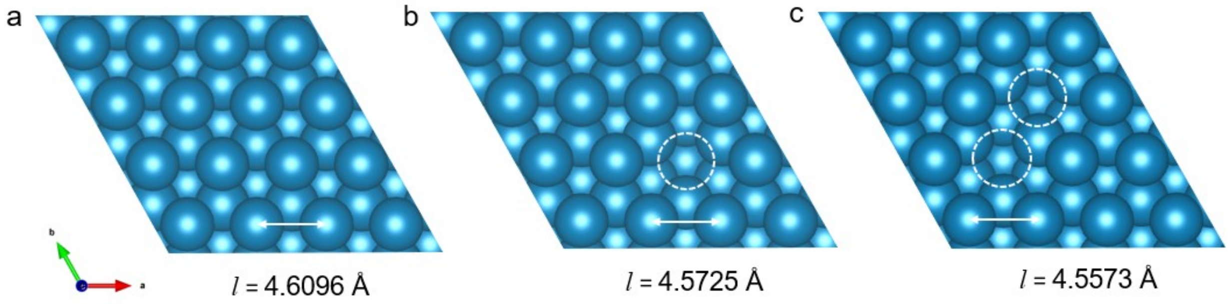

Figure S19. Optimized structure of perfect Bi, Bi-V_1 and Bi-V_2 (*l* is the bond length).

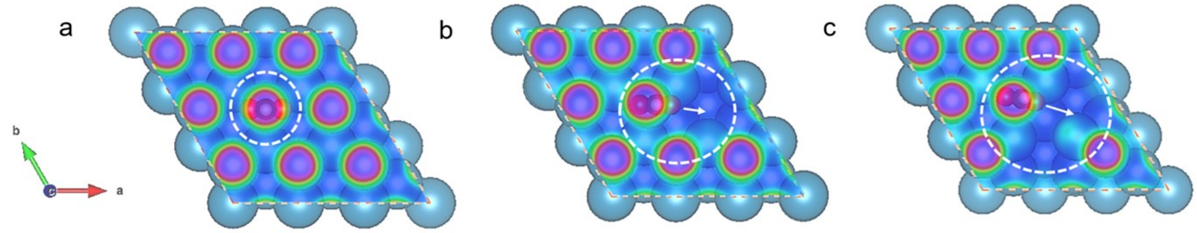

Figure S20. The overlap view of electron local functions and the optimized models of adsorbed *OHCO on Bi atoms: (a) perfect Bi; (b) Bi-V_1; (c) Bi-V_2.

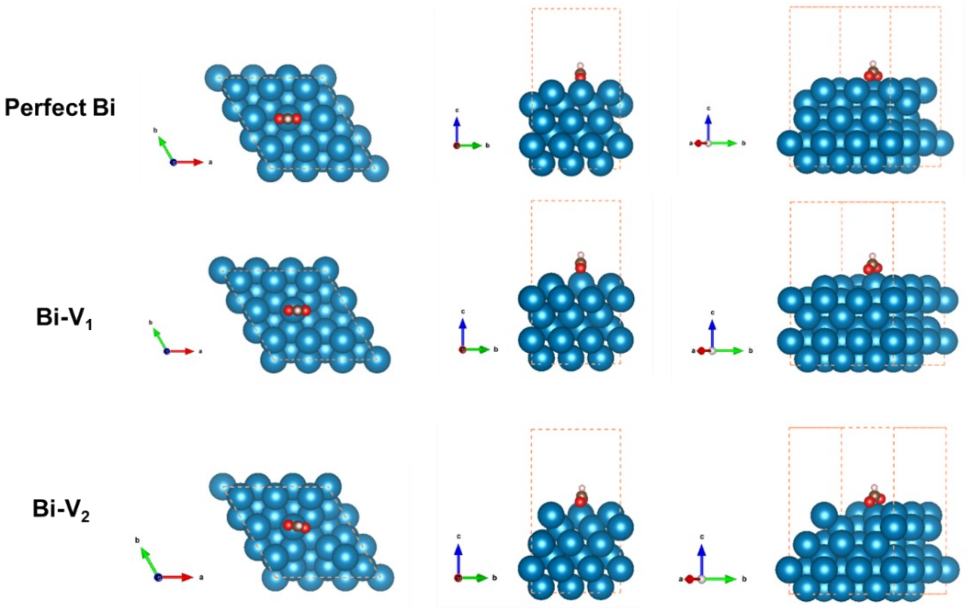

Figure S21. The optimized structures of *OCHO adsorbed on perfect Bi, Bi-V$_1$ and Bi-V$_2$ from different views.

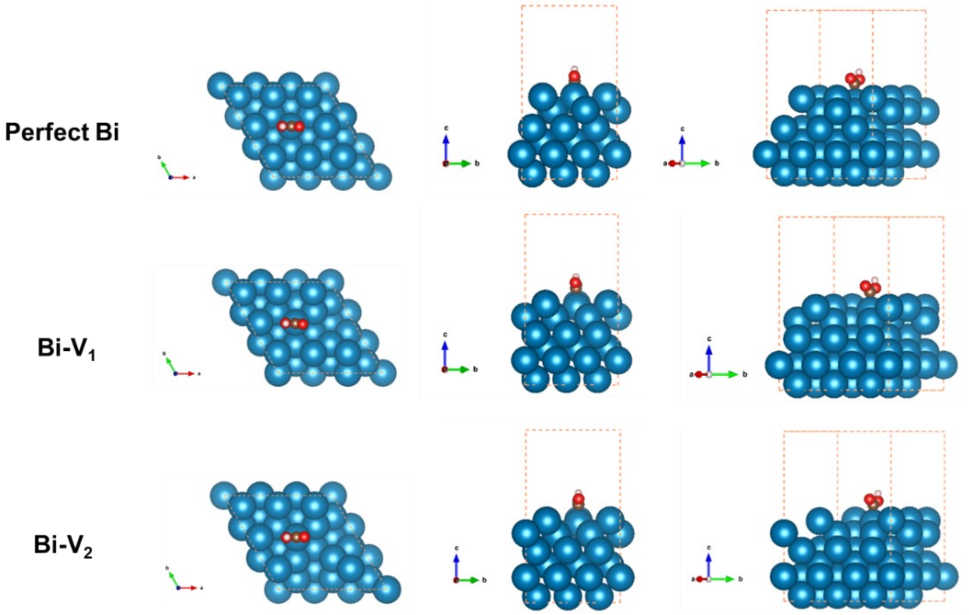

Figure S22. The optimized structures of *COOH adsorbed on perfect Bi, Bi-V$_1$ and Bi-V$_2$ from different views.

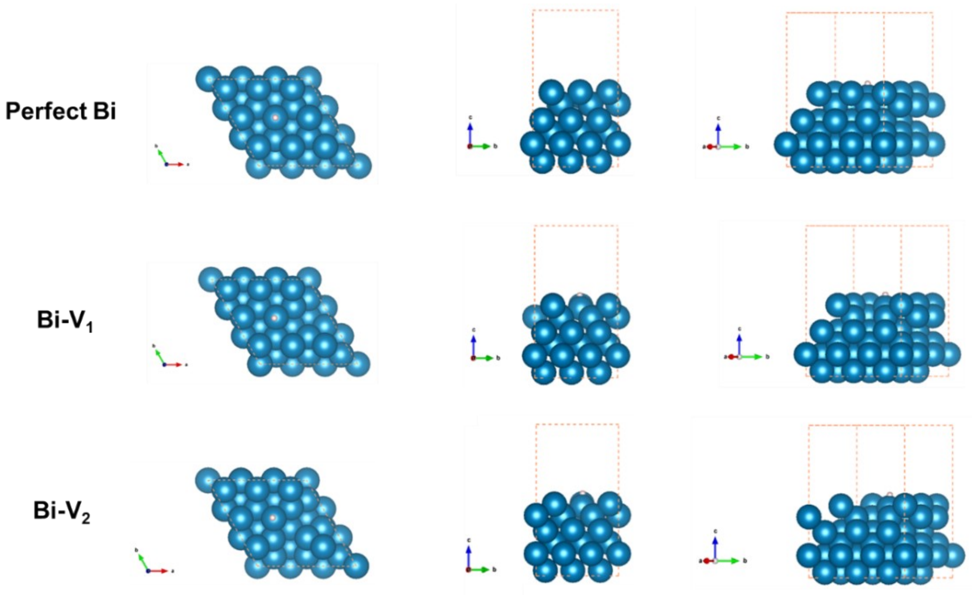

Figure S23. The optimized structures of *H adsorbed on perfect Bi, Bi-V$_1$ and Bi-V$_2$ from different views.

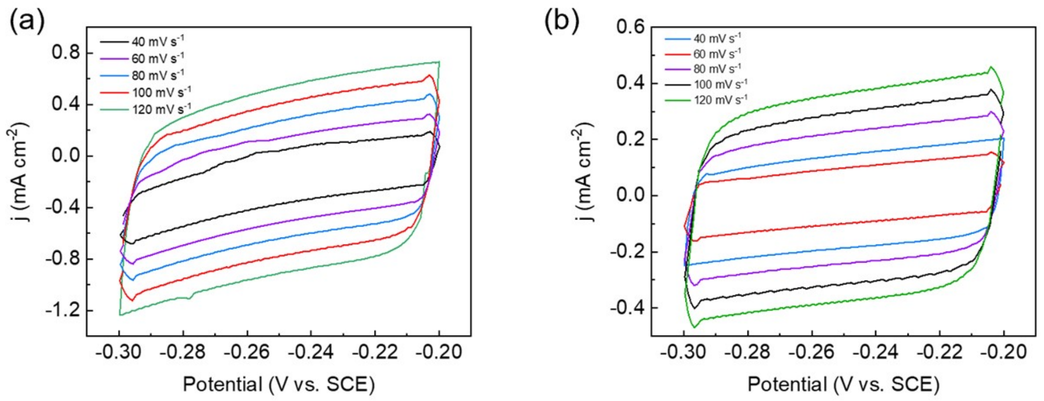

Figure S24. Cyclic voltammograms (CVs) of (a) Bi_5O_7I NTs and (b) Bi_5O_7I NBs stripping between -0.3 and -0.2 V vs. SCE in CO_2-saturated 0.5 M $KHCO_3$.

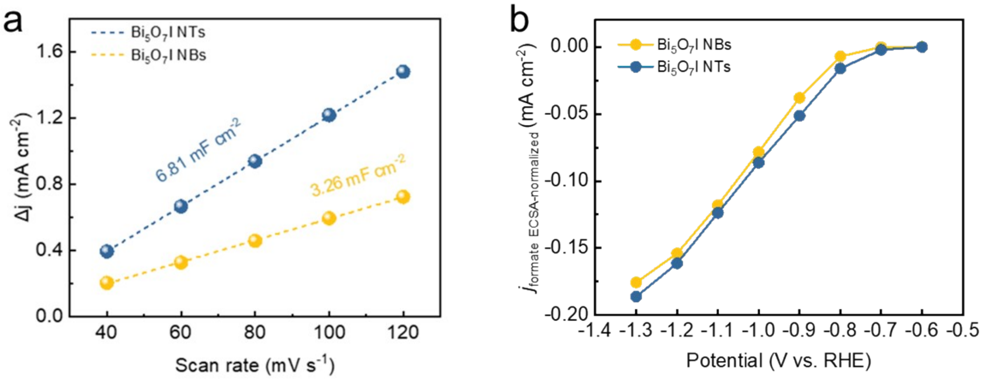

Figure S25. (a) Charging current density differences (Δj) plotted against scan rates and (b) ECSA normalized partial current of formate ($j_{\text{formate ECSA-normalized}}$) for Bi_5O_7I NTs and NBs.

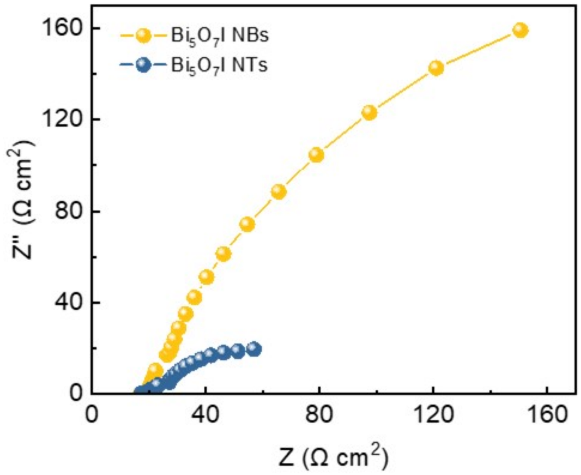

Figure S26. Nyquist plots of the electrochemical impedance spectra for Bi_5O_7I NTs and Bi_5O_7I NBs at -1.0 V vs. RHE in CO_2-satured 0.5 M $KHCO_3$ electrolyte.

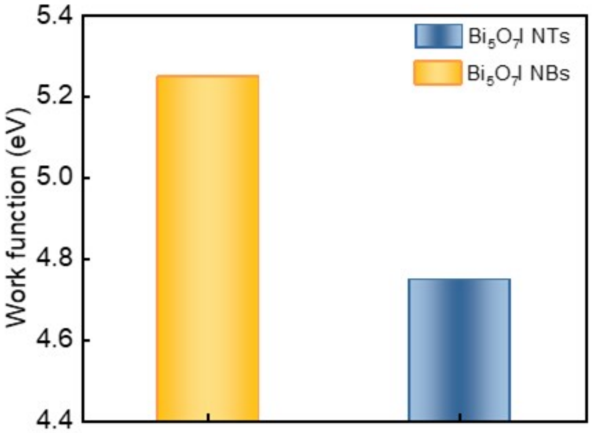

Figure S27. The calculated work functions of Bi_5O_7I NTs and NBs based on experimental measurements.

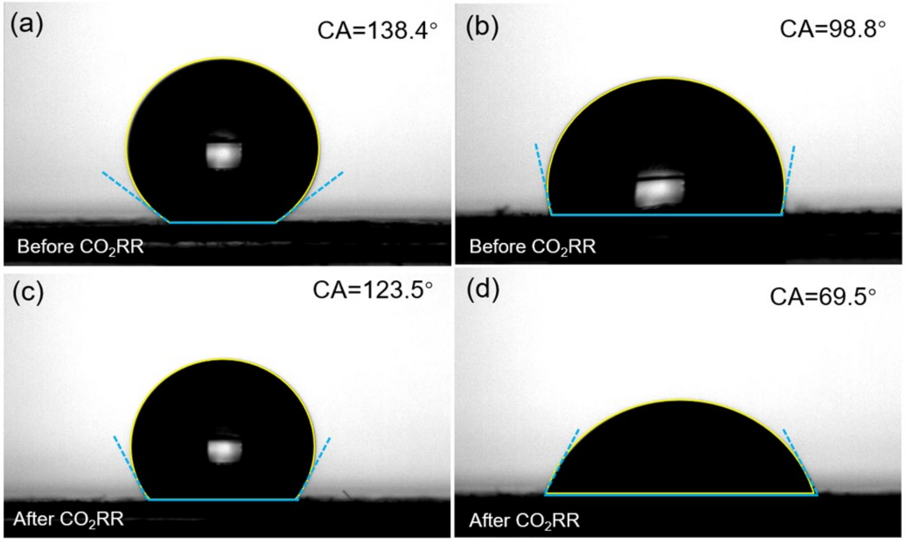

Figure S28. Images of contact angle measurement for (a) and (c) Bi_5O_7I NTs, (b) and (d) Bi_5O_7I NBs before and after CO_2RR.

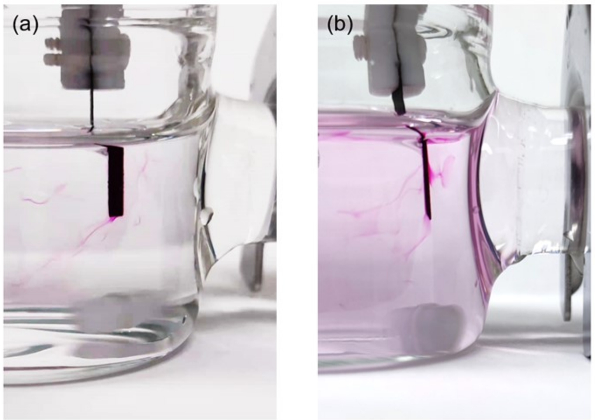

Figure S29. Phenolphthalein color transition experiment. Photographs of the phenolphthalein color transition experiment for (a) Bi_5O_7I NBs and (b) Bi_5O_7I NTs at -1.0 V vs RHE.

The phenolphthalein color transition experiment was performed on the catalysts to observe the local pH effect. 0.05 M phenolphthalein in ethanol was added into the CO_2-saturated 0.5 M $KHCO_3$ close to the electrode. After 15 s electrolysis at -1.0 1vs RHE, the color near the electrode changes to obvious pink on Bi_5O_7I NTs electrode, implying the higher local pH around the cathode.

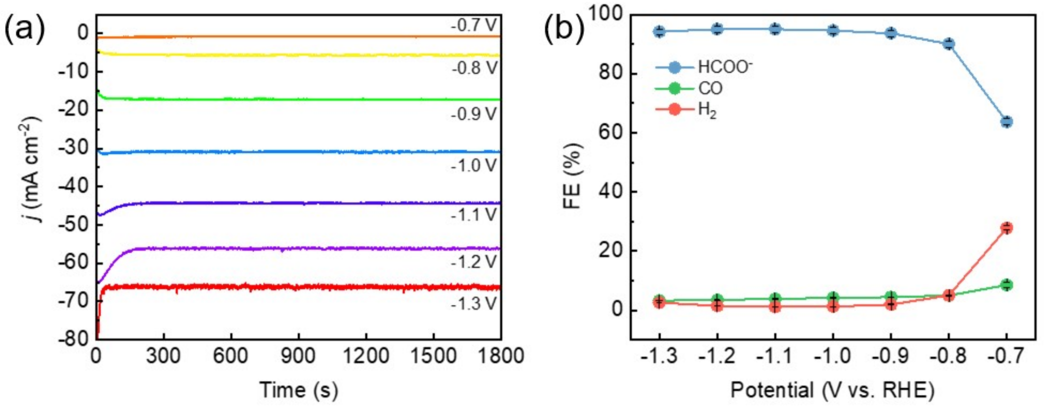

Figure S30. Plots of current densities as a function of time and Faradaic efficiencies at different potentials on Bi_5O_7I NTs in CO_2-saturated 0.5 M NaCl.

Table S1. Summary and comparison of recently reported Bi-based electrocatalysts for CO_2RR to formate formation in H-type cell.

Catalyst	**Electrolyte**	**Maximum $FE_{formate}$ with the applied potential (vs. RHE)**	**Potential window for $FE_{formate}$ > 90%**	**Ref.**
Bi-NRs@NCNTs	0.1 M $KHCO_3$	90.9 % at -0.9 V	<100	[9]
PD-Bi1	0.5 M $KHCO_3$	91.4 % at -0.9 V	<100	[10]
Bi@Sn NPs	0.5 M $KHCO_3$	91 % at -1.1 V	<100	[11]
Bi-MOF	0.1 M $KHCO_3$	92.2 % at -0.9 V	<100	[12]
Bi(btb)	0.5 M $KHCO_3$	95.3 % at -0.97 V	200	[13]
Bi_2O_3@C-800	0.5 M $KHCO_3$	92 % at -0.9 V	100	[14]
Bi NTs	0.5 M $KHCO_3$	97 % at -1.0 V	450	[15]
Bi-SnO_x	0.5 M $KHCO_3$	95.8 % at -0.88 V	250	[16]
f-Bi_2O_3	0.1 M $KHCO_3$	87 % at -1.2 V	<100	[17]
Bi_2O_3NSs@MCCM	0.1 M $KHCO_3$	93.8 % at -1.256 V	<100	[18]
Bi-Sn aerogel	0.1 M $KHCO_3$	93.9 % at -1.0 V	300	[19]
BOC@GDY	0.5 M $NaHCO_3$	95.5 % at -0.85 V	150	[20]
Bi_5O_7I NTs	**0.5 M $KHCO_3$**	**94.2 % at -1.3 V** **94.3% at -1.2 V** **94.3% at -1.1 V** **95.5% at -1.0 V** **93.6% at -0.9 V** **92.3% at -0.8 V**	**500**	**This work**

Table S2. Summary and comparison of recently reported electrocatalysts for CO_2RR to formate formation in a flow cell.

Catalyst	**Electrolyte**	**Maximum $FE_{formate}$ with the applied potential (vs. RHE)**	**Potential window (mV)**	**Ref.**
Bi@Sn NPs	2.0 M $KHCO_3$	95% at -1.02 V	350 ($FE_{formate} > 90\%$)	[11]
BOC NFs	1.0 M KOH	98.7% at 0.8 V	1200 ($FE_{formate} > 90\%$)	[21]
Bi_2O_3@C-800	1.0 M KOH	95% at -0.7 V	700 ($FE_{formate} > 90\%$)	[14]
S-$BiVO_4$	1.0 M $KHCO_3$	97.5 % at -1.0 V	750 ($FE_{formate} > 90\%$)	[22]
SnO_2-Bi_2O_3	1.0 M KOH	91% at -1.29 V	100 ($FE_{formate} > 90\%$)	[23]
BOC@GDY	1.0 M KOH	97% at -0.85 V	450 ($FE_{formate} > 90\%$)	[20]
Bi_2S_3-Bi_2O_3 NSs	1.0 M KOH	95% at -1.0 V	800 ($FE_{formate} > 90\%$)	[24]
MIL-68(In)-NH_2	1.0 M KOH	94.4% at -1.1 V	300 ($FE_{formate} > 90\%$)	[25]
In-Sn alloy	1.0 M KOH	94% at -0.98 V	550 ($FE_{formate} > 90\%$)	[26]
SnS	1.0 M KOH	88 ± 2% at -1.3 V	300 ($FE_{formate} > 80\%$)	[27]
SnO_2/Sn	1.0 M KOH	93% at -0.98 V	500 ($FE_{formate} > 90\%$)	[28]
$ZnIn_2S_4$	1.0 M $KHCO_3$	99.3% at -1.18 V	300 ($FE_{formate} > 90\%$)	[29]
Sn_3O_4	1.0 M KOH	91.1% at -1.02 V	300 ($FE_{formate} > 80\%$)	[30]
Bi_5O_7I NTs	**1.0 M KOH**	**97.5% (-1.0 V)**	**1000 ($FE_{formate} > 93\%$)**	**This work**

Table S3. Summary and comparison of recently reported electrocatalysts for CO_2RR to formate formation in MEA.

Catalyst	E_{cell} (V)	j_{cell} (mA cm^{-2})	FE_{max} (%)	Time (h)	Ref.
2D-Bi	3	30	80	100	[31]
Bi NS	3	200	97	110	[32]
Bi_2O_3/BiO_2	3.7	220	95.4	30	[33]
InN-C	3	64.2	90	88	[34]
BiIn alloy NPs	3.6	120	92	27	[35]
h-In_2O_3	3.6	150	85	100	[36]
Bi_5O_7I NTs	**3.5**	**200**	**97.5**	**140**	**This work**

References

[1] G. Kresse, J. Hafner, *Phys. Rev. B* **1993**, *47*, 558-561.

[2] G. Kresse, J. Hafner, *Phys. Rev. B* **1994**, *49*, 14251-14269.

[3] G. Kresse, J. Furthmüller, *Phys. Rev. B* **1996**, *54*, 11169-11186.

[4] B. Hammer, L. B. Hansen, J. K. Nørskov, *Phys. Rev. B* **1999**, *59*, 7413-7421.

[5] H. J. Monkhorst, J. D. Pack, *Phys. Rev. B* **1976**, *13*, 5188-5192.

[6] V. Tripković, E. Skúlason, S. Siahrostami, J. K. Nørskov, J. Rossmeisl, *Electrochim. Acta* **2010**, *55*, 7975-7981.

[7] C. J. Cramer, *Essentials of computational chemistry: theories and models*, John Wiley & Sons, England, **2013**.

[8] W. J. Durand, A. A. Peterson, F. Studt, F. Abild-Pedersen, J. K. Nørskov, *Surf. Sci.* **2011**, *605*, 1354-1359.

[9] W. Zhang, S. Yang, M. Jiang, Y. Hu, C. Hu, X. Zhang, Z. Jin, *Nano Lett.* **2021**, *21*, 2650-2657.

[10] Y. Wang, Y. Li, J. Liu, C. Dong, C. Xiao, L. Cheng, H. Jiang, H. Jiang, C. Li, *Angew. Chem. Int. Ed.* **2021**, *60*, 7681-7685.

[11] Y. Xing, X. Kong, X. Guo, Y. Liu, Q. Li, Y. Zhang, Y. Sheng, X. Yang, Z. Geng, J. Zeng, *Adv. Sci.* **2020**, 1902989.

[12] F. Li, G. H. Gu, C. Choi, P. Kolla, S. Hong, T.-S. Wu, Y.-L. Soo, J. Masa, S. Mukerjee, Y. Jung, J. Qiu, Z. Sun, *Appl. Catal. B-Environ.* **2020**, *277*, 119241.

[13] P. Lamagni, M. Miola, J. Catalano, M. S. Hvid, M. A. H. Mamakhel, M. Christensen, M. R. Madsen, H. S. Jeppesen, X. M. Hu, K. Daasbjerg, T. Skrydstrup, N. Lock, *Adv. Funct. Mater.* **2020**, 1910408.

[14] P. Deng, F. Yang, Z. Wang, S. Chen, Y. Zhou, S. Zaman, B. Y. Xia, *Angew. Chem. Int. Ed.* **2020**, *59*, 10807-10813.

[15] K. Fan, Y. Jia, Y. Ji, P. Kuang, B. Zhu, X. Liu, J. Yu, *ACS Catal.* **2019**, *10*, 358-364.

[16] Q. Yang, Q. Wu, Y. Liu, S. Luo, X. Wu, X. Zhao, H. Zou, B. Long, W. Chen, Y. Liao, L. Li, P. K. Shen, L. Duan, Z. Quan, *Adv Mater* **2020**, e2002822.

[17] T. Tran-Phu, R. Daiyan, Z. Fusco, Z. Ma, R. Amal, A. Tricoli, *Adv. Funct. Mater.* **2019**, *30*, 1906478.

[18] S. Liu, X. F. Lu, J. Xiao, X. Wang, X. W. D. Lou, *Angew. Chem. Int. Ed.* **2019**, *58*, 13828-13833.

[19] Z. Wu, H. Wu, W. Cai, Z. Wen, B. Jia, L. Wang, W. Jin, T. Ma, *Angew. Chem. Int. Ed.* **2021**, *60*, 12554-12559.

[20] S.-F. Tang, X.-L. Lu, C. Zhang, Z.-W. Wei, R. Si, T.-B. Lu, *Sci. Bull.* **2021**, *66*, 1533-1541.

[21] P. F. Sui, M. R. Gao, S. Liu, C. Xu, M. N. Zhu, J. L. Luo, *Adv. Funct. Mater.* **2022**, 2203794.

[22] W. Ma, J. Bu, Z. Liu, C. Yan, Y. Yao, N. Chang, H. Zhang, T. Wang, J. Zhang, *Adv. Funct. Mater.* **2020**, 2006704.

[23] X. Wang, W. Wang, J. Zhang, H. Wang, Z. Yang, H. Ning, J. Zhu, Y. Zhang, L. Guan, X. Teng, Q. Zhao, M. Wu, *Chem. Eng. J.* **2021**, *426*, 131867.

[24] P. F. Sui, C. Xu, M. N. Zhu, S. Liu, Q. Liu, J. L. Luo, *Small* **2021**, e2105682.

[25] Z. Wang, Y. Zhou, C. Xia, W. Guo, B. You, B. Y. Xia, *Angew. Chem. Int. Ed.* **2021**, *60*, 19107-19112.

[26] J. Wang, S. Ning, M. Luo, D. Xiang, W. Chen, X. Kang, Z. Jiang, S. Chen, *Appl. Catal. B-Environ.* **2021**, *288*, 119979.

[27] J. Zou, C. Y. Lee, G. G. Wallace, *Adv. Sci.* **2021**, *8*, e2004521.

[28] S. Ning, J. Wang, D. Xiang, S. Huang, W. Chen, S. Chen, X. Kang, *J. Catal.* **2021**, *399*, 67-74.

[29] L. P. Chi, Z. Z. Niu, X. L. Zhang, P. P. Yang, J. Liao, F. Y. Gao, Z. Z. Wu, K. B. Tang, M. R. Gao, *Nat. Commun.* **2021**, *12*, 5835.

[30] L.-X. Liu, Y. Zhou, Y.-C. Chang, J.-R. Zhang, L.-P. Jiang, W. Zhu, Y. Lin, *Nano Energy* **2020**, *77*, 105296.

[31] C. Xia, P. Zhu, Q. Jiang, Y. Pan, W. Liang, E. Stavitski, H. N. Alshareef, H. Wang, *Nat. Energy* **2019**, *4*, 776-785.

[32] Y. Yuan, Q. Wang, Y. Qiao, X. Chen, Z. Yang, W. Lai, T. Chen, G. Zhang, H. Duan, M. Liu, H. Huang, *Adv. Energy Mater.* **2022**, 2200970.

[33] X. Feng, H. Zou, R. Zheng, W. Wei, R. Wang, W. Zou, G. Lim, J. Hong, L. Duan, H. Chen, *Nano Lett* **2022**.

[34] P. Hou, X. Wang, P. Kang, *J. CO_2 Util.* **2021**, *45*, 101449.

[35] K. Yao, H. Wang, X. Yang, Y. Huang, C. Kou, T. Jing, S. Chen, Z. Wang, Y. Liu, H. Liang, *Appl. Catal. B* **2022**, *311*, 121377.

[36] Z. Liu, X. Lv, J. Zhang, A. Guan, C. Yang, S. Yan, Y. Chen, K. Liu, G. Zheng, *Adv. Mater. Interfaces* **2022**, *9*, 2101956.